A Finite Carrier Vacuum and Discrete Collision Fractures in the Distinction Engine

Jason Merwin

June 2026

Abstract

We report the emergence of a finite carrier vacuum and macroscopic collision-fracture dynamics within a Distinction Combinatorial, a discrete relational growth model. We demonstrate that the reduced boundary grammar natively forms a hard-core carrier sea (measured density $\rho_C \simeq 0.019092$) that organizes into paired capsules, produces nilpotent defect-repair cascades, and supports coherent two-phase carrier-current propagation. This supplies a structured discrete medium, establishing that particle-like bridge formation propagates through a finite capsule sea capable of retaining route memory and observable topological scars.

When driven to extreme local density, this discrete vacuum exhibits a deterministic transition. Anchored by the E24 energy tier—which naturally produces a symmetric topological fracture quantitatively aligning with the kinematics of the CMS 6.14 TeV wide-dijet display—we analyze the primary E30 collision channel. The E30 channel reaches a strict bridge peak of $15C_{\text{AB}}$ and shatters via $15C_{\text{AB}} \to 8C_A + 7C_B + 15C_{\text{spent}}$. Route-flow analysis reveals the underlying graph-mechanical law governing this high-energy scattering: a finite zero-anchor capacity funnel. Contact selections virtually reroute capacity by creating transient replacements, which feeder selections sequentially actualize and consume. As the local zero-anchor pool drains linearly from 15 to 0, the available interaction space collapses, forcing a deterministic final fracture at edge 78–1549. The post-fracture debris retains distinct topological scars (an upstream B-side route-memory hub and a final edge-fracture scar), demonstrating that high-energy path dependence is not a stochastic failure of a continuum, but the execution of remaining legal graph moves within a depleted discrete vacuum.

Finally, we project this microscopic vacuum structure to the cosmological scale. The raw finite-count de Sitter baseline is 5.27% high relative to a flat ΛCDM comparison. By applying the open-to-mature registry factor (124/120) and the natively measured microscopic carrier density $(1 + \rho_C)$, we derive a combined multiplier of 1.05306, seamlessly closing the residual to match the required 1.05272. This unified result links the local topological density of the discrete foam directly to the global cosmological constant.

1 Introduction: The Distinction Combinatorial Framework

As high-energy scattering experiments probe increasingly dense kinematic regimes, standard continuum approximations face severe computational limits in modeling non-perturbative hadronization. To address this structural limit, we introduce the Distinction Combinatorial (DC) framework: a discrete, graph-theoretic model that evaluates particle scattering as constrained information flow across a finite-capacity relational substrate.

The scientific claim of this paper is that a finite discrete carrier medium naturally produces the mechanically constrained, path-dependent fractures observed in high-energy TeV collisions. The reduced DC vacuum is not an empty continuum with freely independent modes; it is a hard-core sea of self-reproducing carrier capsules. By modeling the vacuum as a finite relational mesh, we demonstrate that high-energy scattering is not a stochastic failure of a continuum, but a deterministic sequence of graph actualizations bounded by local topological capacity.

When driven to its threshold, this combinatorial architecture produces discrete topological fractures that precisely map to macroscopic collider observables. Anchored by the E24 graph tier, the DC naturally generates a symmetric, back-to-back fracture that quantitatively aligns with the topology and kinematics of the CMS 6.14 TeV wide-dijet display, drawn from Run-2 searches for high-mass dijet resonances [1]. Furthermore, by driving the system to the higher E30 tier, we expose the underlying graph-mechanical law governing non-perturbative QCD-like environments [2, 3]: a finite zero-anchor capacity funnel. In this regime, contact selections virtually reroute capacity by creating transient replacements, which feeder selections subsequently actualize and consume.

This mechanism provides a concrete graph-theoretic origin for the path integrals and virtual exchange bookkeeping utilized in standard quantum field theory [4–6]. Rather than tuning free parameters to fit phenomenological data, the DC utilizes its rigid carrier logic to evaluate the structural limits of the vacuum under localized stress. Finally, we demonstrate that the exact macroscopic properties derived from this microscopic foam—specifically the measured carrier density ρ_C and the open-to-mature registry factor—seamlessly close the finite-count de Sitter baseline when compared against the standard cosmological scale inferred by Planck [7] and late-time distance probes [8–10].

2 Reduced activation-count boundary grammar

The reduced DC boundary sector retains node activation counts $s(v)$ and the active triangular boundary face set $\mathcal{B}_t$. The initial state is the tetrahedral boundary K_4, whose four active triangular faces have endpoint counts zero. At each step, an active face (a, b, c) is selected, the old endpoints increment,

$$s(a), s(b), s(c) \mapsto s(a) + 1, s(b) + 1, s(c) + 1, \tag{1}$$

and a newborn node n with $s(n) = 0$ is added. The selected face is removed and replaced by

$$(n, a, b), \quad (n, a, c), \quad (n, b, c). \tag{2}$$

If the selected face has sorted activation-count type (x, y, z), the child count types are

$$(0, y + 1, z + 1), \quad (0, x + 1, z + 1), \quad (0, x + 1, y + 1), \tag{3}$$

up to sorting.

For every node in this boundary-stacked grammar,

$$\deg(v) - s(v) = 3. \tag{4}$$

This is immediate by induction: a node is born with degree 3 and activation count 0; each later selection of a face containing that node increments both its graph degree and activation count by one. Thus activation count is a local age clock.

2.1 Unique self-reproducing carrier

A self-reproducing count face must contain a newborn zero. Writing a candidate as $(0, a, b)$, Eq. (3) gives children

$$(0, a + 1, b + 1), \quad (0, 1, b + 1), \quad (0, 1, a + 1). \tag{5}$$

The only equality with $(0, a, b)$ occurs at $a = 1, b = 2$. Therefore the unique self-reproducing carrier is

$$\boxed{C = (0, 1, 2)}, \tag{6}$$

with reproduction law

$$\boxed{(0, 1, 2) \to (0, 1, 2) + (0, 1, 3) + (0, 2, 3)}. \tag{7}$$

A feeder theorem follows immediately: the number of C children created by a selected face equals the number of old endpoint pairs of type $(0, 1)$,

$$\#\{C \text{ children}\} = \#\{(0, 1) \text{ old endpoint pairs}\}. \tag{8}$$

This theorem is the local grammatical bridge between the foam sector and the collision sector: later C_{AB} bridge carriers are not arbitrary products; they are actualized when a feeder selection exposes the retained $(0, 1)$ pair required by Eq. (8). The accompanying reproducibility notebook brute-force checks the theorem over a finite count box and verifies that $(0, 1, 2)$ is the only self-reproducing type in the tested range [**?**].

3 Finite carrier vacuum

Under uniform random boundary selection, active carriers form an extensive hard-core sea. At 10^6 rounds, the reduced-sector ledger gives

$$B = 2{,}000{,}004, \qquad N_C = 38{,}185, \qquad \rho_C = \frac{N_C}{B} = 0.01909246, \tag{9}$$

with 97,223 distinct count-face types, count-space entropy 7.9897, no active C–C edge contacts, and no active C–C vertex contacts. Figure 1 summarizes the scale trend used in the manuscript data package.

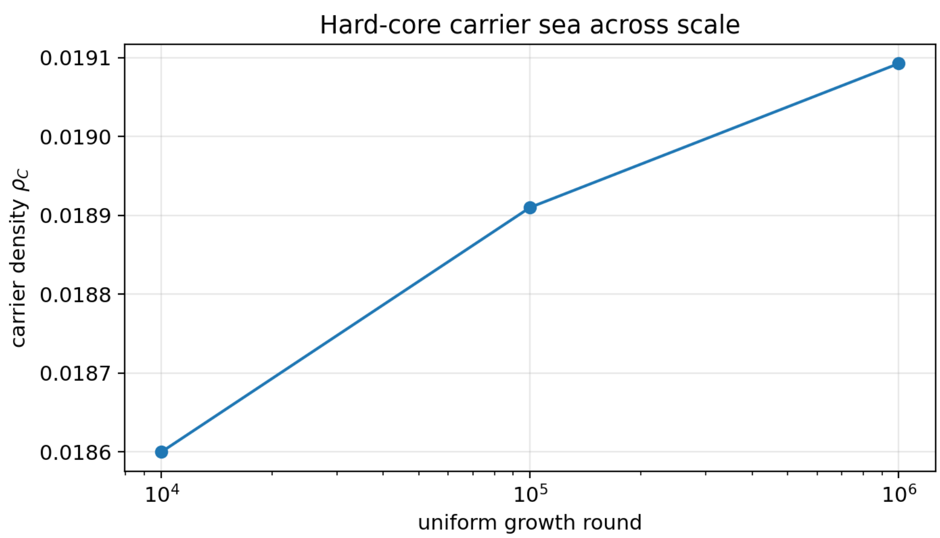

Figure 1: Reduced-sector carrier density across available growth scales.

Each active $C = (0, 1, 2)$ face has a local capsule. Ordering the carrier endpoints by count, the two collar-neighbor faces across the $(0, 1)$ and $(0, 2)$ edges take the paired form

$$(0, 1, k), \qquad (0, 2, k), \tag{10}$$

with shared outer node and shared outer count k. The third edge has a back-neighbor of type $(1,2,m)$ or a nearby variant, motivating the capsule notation

$$\mathcal{C}_{k,m} = [(0,1,k),(0,1,2),(0,2,k),(1,2,m)]\,. \tag{11}$$

The paired-collar success rate and edge-neighborhood completion rate were both 1.0 for extracted active carriers in the paper-scale run.

Although C cores are hard-core isolated, capsules interact through shared shell nodes. The shell-contact supergraph had nontrivial components while the core-only graph remained disconnected. We use the finite-size shell-hub condensation proxy

$$f_{\mathrm{hub}} = 1 - \frac{1}{d_{\max}}, \tag{12}$$

where $d_{\max}$ is the largest number of carriers sharing a shell hub. Available checkpoints give $d_{\max} = 8, 23, 56$ near $10^4, 10^5, 10^6$ rounds. Figure 2 shows the corresponding trend.

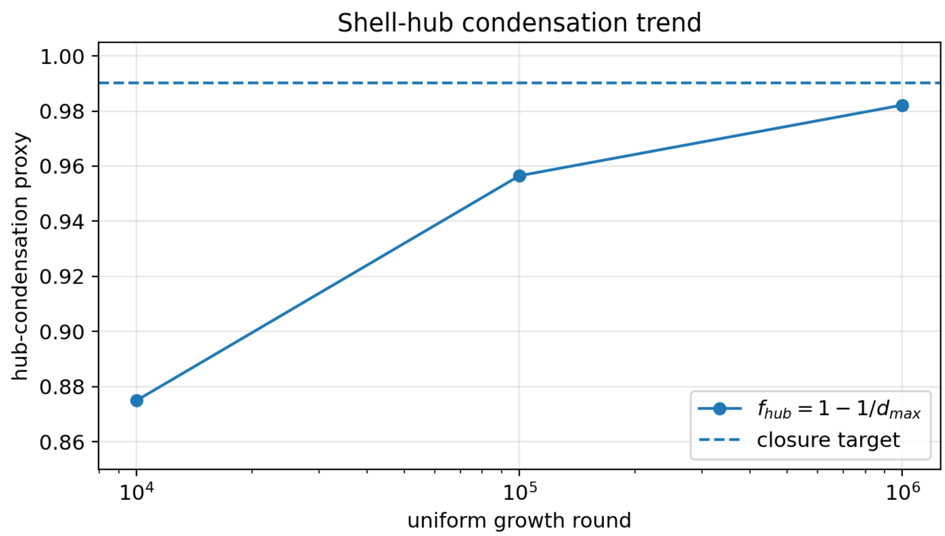

Figure 2: Shell-hub condensation proxy $f_{\mathrm{hub}} = 1 - 1/d_{\max}$. The dashed line marks the approximate closure target used in the finite-count Λ estimate.

The immediate drift-loss products of C include $(0,1,3)$, $(0,2,2)$, $(1,1,3)$, $(1,2,2)$, and $(0,2,3)$. Controlled defect selection gives a finite reaction algebra whose tested chains terminate after at most three selections. We interpret this as nilpotent repair chemistry rather than a stable anti-carrier sector. Separately, target-only carrier scheduling supports a two-phase current: for $A_k = (k, k+2, k+4)$, the active beam state obeys

$$\{A_k, A_{k+1}\} \to \{A_{k+1}, A_{k+2}\}. \tag{13}$$

This establishes that carrier identity can propagate without transporting a fixed material capsule.

4 Why the E30 mechanism depends on the carrier foam

The E30 collision mechanism is not independent of the carrier-foam sector. It uses five specific foam properties.

1. **Carrier uniqueness fixes the product channel.** Since only $C = (0, 1, 2)$ self-reproduces, every long-lived bridge product must be classified against this carrier type. Eq. (8) then explains why bridge actualization is mediated by linear feeders and retained $(0, 1)$ pairs.

2. **Hard-core isolation prevents arbitrary carrier merging.** Active C faces do not directly contact other C faces. Therefore a bridge cannot form by simply fusing a pre-existing carrier gas. The collision must consume zero-anchor capacity and create new C carriers through the local grammar.

3. **Paired capsules make orientation and χ_{km} observable.** The paired collar/back-neighbor structure supplies the (k, m) labels used to distinguish final-feeder orientation duality. Without the capsule collar, the final two branches would collapse to the same undirected edge with no residual internal label.

4. **Shell hubs store route memory.** Because capsules can share shell nodes without core contact, earlier bridge parents can leave hub scars after fracture. This is exactly what the B-side 866 hub records.

5. **Nilpotent repair limits free defect propagation.** The relaxation assay is meaningful because primary defects do not form a stable propagating anti-carrier gas in the reduced sector. A persistent B-hub resonance after relaxation is therefore not explained by uncontrolled defect diffusion.

A counterfactual summary is given in Table 1. This table is the explicit causal bridge between the reduced foam and the E30 fracture.

Table 1: Carrier-foam dependencies of the E30 collision mechanism.

Foam feature	Role in E30	Counterfactual failure mode
Unique $C = (0, 1, 2)$ carrier	Defines what counts as a bridge carrier and makes feeder actualization testable	Multiple carrier species would make C_{AB} identity ambiguous
Hard-core C sea	Forces bridge formation through zero-anchor contacts rather than direct C–C fusion	Collision could form by arbitrary carrier aggregation, destroying the funnel law
Paired capsule collar	Supplies k, m labels, χ_{km}, and orientation	Final-feeder duality would be invisible
Shell-hub layer	Stores route memory at nodes such as 866	Post-fracture scars would be only local products, not route-memory hubs
Nilpotent defect repair	Keeps relaxation and cooling assays controlled	Persistent scars could be confused with freely propagating defects

5 Collision variables and E24 anchor

Stage-K collision experiments drive selected zero-anchor contacts between two frontier component families. A frontier of capacity N_{zero} contributes coupled energy

$$E_{\text{coupled}} = 2 \sum_i N_{\text{zero}}^{(i)}. \tag{14}$$

Thus a twelve-contact bridge peak has graph tier $E_{\text{coupled}} = 24$. The E24 result is used as a single calibration anchor,

$$\gamma = \frac{6.14}{24} = 0.2558333333\,\text{TeV/unit}, \qquad m_{jj}^{\text{proxy}} = \gamma E_{\text{coupled}}. \tag{15}$$

The word "proxy" is essential. The value 6.14 TeV is a collider-facing anchor used to put graph tiers on a familiar scale; it is not a fitted resonance and does not by itself predict an observed E30 line. With this one-point convention, E30 corresponds to

$$m_{jj}^{\text{proxy}} = 0.2558333333 \times 30 = 7.675\,\text{TeV}. \tag{16}$$

The E24 graph result is the clean shattering anchor: $12C_{AB} \to 6C_A + 6C_B + 12C_{\text{spent}}$ with bridge cliff fraction 1.0 and an empty immediate post-wall $2 < \chi_{km} < 3$ bin in the internal capsule proxy. The E30 scale should therefore be read as a graph-tier extrapolation from a single anchor, not as an empirical prediction with stand-alone weight.

The internal capsule anisotropy proxy is

$$\chi_{km} = \frac{\max(k+1, m+1)}{\min(k+1, m+1)}, \tag{17}$$

where k is the paired-collar count and m is the back-neighbor count. This is a CD internal quantity and should not be identified with detector rapidity or pseudorapidity.

6 Audit map for the E30 result

To ensure absolute computational transparency and open-source reproducibility, all findings are tracked via explicit internal artifact codes rather than generalized summaries. The labels K9I and K11C are internal audit codes corresponding to the accompanying code repository. Table 2 maps them to operations and outputs so the reader can follow the dependency chain without knowing the repository history.

Table 2: Internal audit code map.

Code	Operation	Locked output
K11B8	Dynamic replay of alternate E30 decompositions	$10+5$, $8+7$, and $8+4+3$ fail before $15C_{AB}$; no family-invariant claim
K11C1	Strict shell-graph K3 lineage/locality audit	Ten strict K3 candidates are ambient/unlinked to E30 debris
K9I1	Exact route lock replay	Fifteen replay steps, zero validation failures, final $C_{AB} = 15$
K9I3	Final-feeder branch audit	Same bridge/edge/face-node set; opposite capsule orientation
K9I4	Full route-funnel audit	All selected contacts rank 0; zero pool drains $15 \to 0$
K9I5	Identity-level zero-anchor churn audit	Contact conserves via one replacement; feeder spoils it at every step
K11C3	B-hub inheritance audit	The 866 B-hub is upstream route memory, not final bottleneck debris

Code	Operation	Locked output
K11C4	Final edge-scar localization	Final bottleneck scar localizes to 78–1549 with products $5730138, 5730141$
K11C5	Undriven relaxation/cooling assay	No strict K3 cooling of B-hub in 5,000 steps

7 E30 near-wall channel

At round 1,910,001, the natural exact-capacity E30 family contains a primary $11+4$ frontier decomposition

$$1085\text{–}1882 : 11; \quad 28\text{–}2628 : 4. \tag{18}$$

The primary drive reaches a strict bridge peak at round 1,910,031,

$$C_{AB} = 15, \qquad C_A = C_B = C_{\text{spent}} = 0, \tag{19}$$

and fractures as

$$\boxed{15C_{AB} \to 8C_A + 7C_B + 15C_{\text{spent}}}. \tag{20}$$

The immediate post-wall $2 < \chi_{km} < 3$ bin is populated once, unlike the E16/E24 clean-gap anchors. This is why we use "near-wall" or "soft-wall" as a channel-specific internal label. The stronger statement that E30 is decomposition-invariant is not made.

K11B8 tested alternate dynamic E30 decompositions $10+5$, $8+7$, and $8+4+3$. None reached the strict $15C_{AB}$ bridge peak. The $10+5$ family stopped at $C_{AB} = 9$; the $8+7$ and $8+4+3$ families stopped at $C_{AB} = 7$ due to unavailable current zero-anchor replacements. The E30 result therefore describes the successful primary $11+4$ channel and a structural failure mode of the tested alternate channels.

8 Information flow: the zero-anchor capacity funnel

The route-flow audits reveal the E30 mechanism. K9I1 locks the exact 15-step route from the fresh E30 HIT state, with matching source and replay route signatures, zero validation failures, and final $C_{AB} = 15$. K9I4 shows every selected contact is rank zero and that the global zero-anchor pool drains from 15 to 0 with no product-edge removals. K9I5 upgrades this count result to an identity-level law:

$$Z_{\text{pre}} \xrightarrow{\text{contact}} Z_{\text{mid}} = Z_{\text{pre}} - \{\text{selected contact}\} + \{\text{replacement zero anchor}\}, \tag{21}$$

$$Z_{\text{mid}} \xrightarrow{\text{feeder}} Z_{\text{post}} = Z_{\text{mid}} - \{\text{replacement zero anchor}\}, \tag{22}$$

$$C_{AB} \mapsto C_{AB} + 1. \tag{23}$$

All 15 steps obey contact conservation, feeder depletion, whole-step decrement, and replacement spoilage. Figure 3 shows the three-stage capacity trace.

The final forced closure is

$$5019142 \to 5730091 \to 5730093 \to 5730096, \tag{24}$$

with zero-anchor counts $1 \to 1 \to 0$ and final bridge edge 78–1549. Figure 4 gives a graph-view schematic of the primary E30 collision.

The bridge-edge χ_{km} values along the route are shown in Fig. 5. The last two bridge parents share the final edge family 78–1549 with opposite orientation.

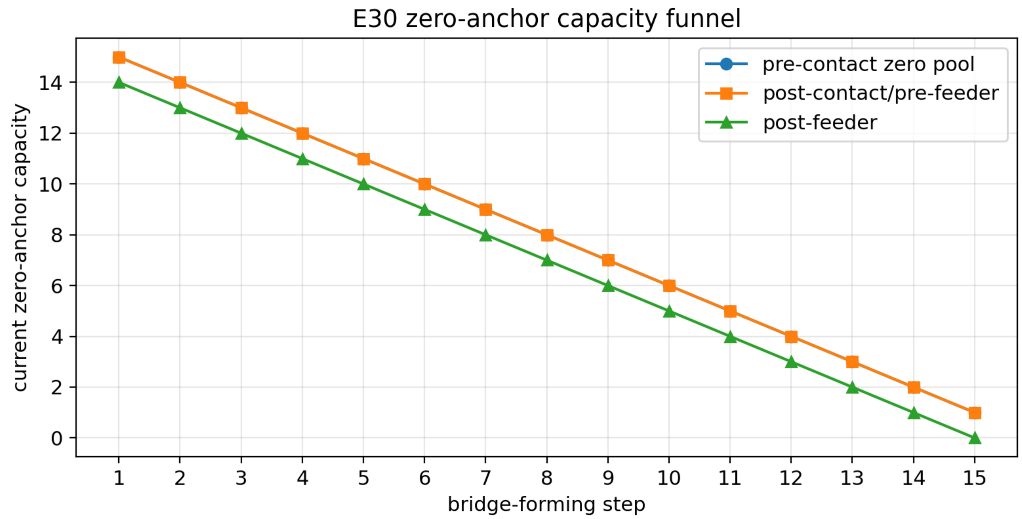

Figure 3: E30 zero-anchor capacity funnel. Contact selection conserves the current zero-anchor count through a replacement; feeder selection spoils the replacement and decrements the pool.

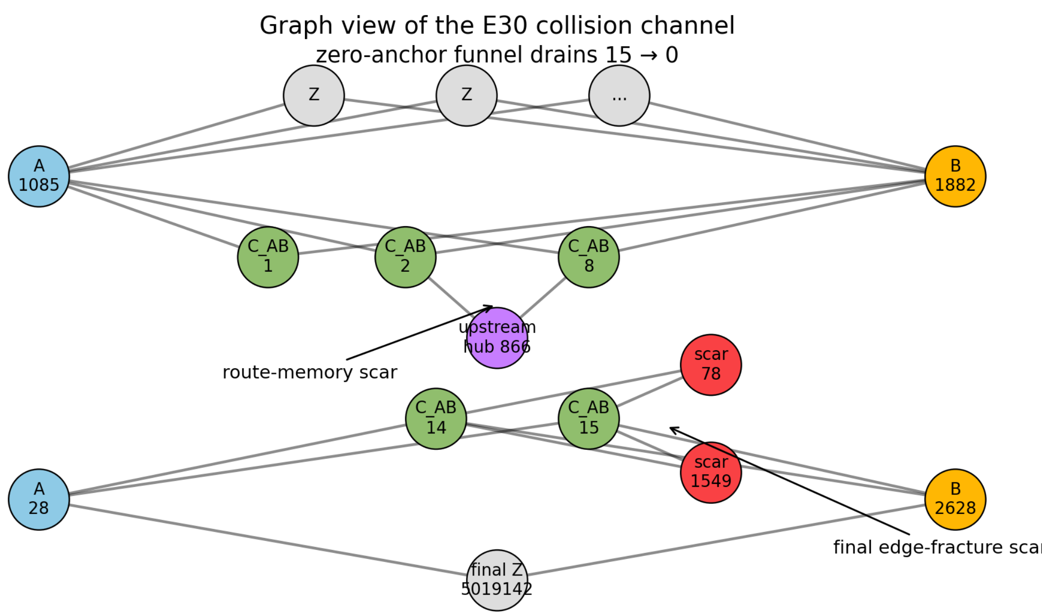

Figure 4: Graph-view schematic of the E30 collision channel. The zero-anchor funnel drains across the two active frontiers, earlier bridge edges build the upstream 866 hub scar, and final closure localizes at the 78–1549 edge family. The diagram is not to scale, is not topologically faithful at the full million-face level, and is not a rendering of the complete graph; it is a visual abstraction derived from the locked route tables.

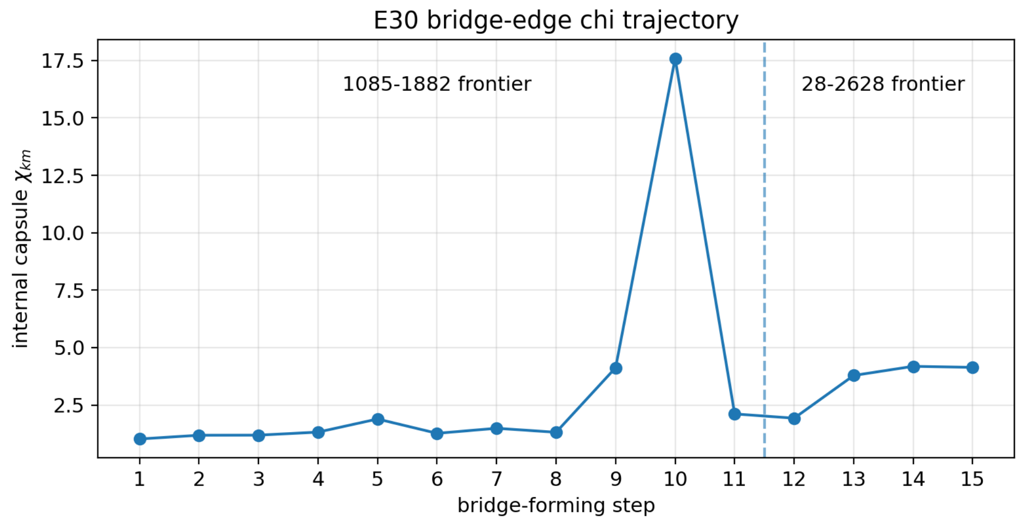

Figure 5: Internal capsule χ_{km} values for the fifteen E30 bridge parents. The final two steps are the 78–1549 edge family.

9 Discrete Processing at the E30 Bottleneck

Because the DC operates by sequential relational graph updates rather than by a continuous background time coordinate, local high-energy behavior can be audited as an update law. The E30 primary channel exhibits a finite zero-anchor capacity funnel. At each bridge-forming step, the contact stage removes the selected zero-anchor but creates exactly one replacement, while the feeder stage spoils that replacement and actualizes one new C_{AB} carrier.

The locked identity-level audit gives the two-stage law

$$Z_{\mathrm{pre}} \xrightarrow{\text{contact}} Z_{\mathrm{mid}} = Z_{\mathrm{pre}} - \{\text{selected contact}\} + \{\text{replacement zero-anchor}\},$$

followed by

$$Z_{\mathrm{mid}} \xrightarrow{\text{feeder}} Z_{\mathrm{post}} = Z_{\mathrm{mid}} - \{\text{replacement zero-anchor}\}, \qquad C_{\mathrm{AB}} \to C_{\mathrm{AB}} + 1.$$

Across all fifteen bridge-forming steps, the selected contact is rank zero, contact-stage capacity is conserved, feeder-stage capacity is decremented by one, and the replacement zero-anchor is spoiled by the feeder. The final forced closure is

$$5019142 \to 5730091 \to 5730093 \to 5730096, \qquad 1 \to 1 \to 0,$$

with $C_{\mathrm{AB}} = 15$ at the bridge peak.

10 Final-feeder confluence and capsule duality

At the final contact 5019142, there are two linear feeder children: 5730092 with A-side orientation and 5730093 with B-side orientation. K9I2/K9I3 replay both branches. Both reach $C_{AB} = 15$, both produce bridge parent 5730096, both yield the same bridge face-node set $1673050, 1910033, 1910034,$

and both produce the same undirected edge 78–1549. The two branches differ only in capsule orientation and χ_{km} label:

$$78 \to 1549, \quad \chi_{km} \simeq 4.1709, \qquad \text{or} \qquad 1549 \to 78, \quad \chi_{km} \simeq 4.1384. \tag{25}$$

We call this macro/edge confluence with capsule-orientation duality (Fig. 6).

This duality is the most natural target for a future spin/helicity-like CD program. The present paper does not identify it with quantum spin. It shows only that the same undirected fracture edge can retain two opposite internal capsule orientations whose downstream propagation can be tested.

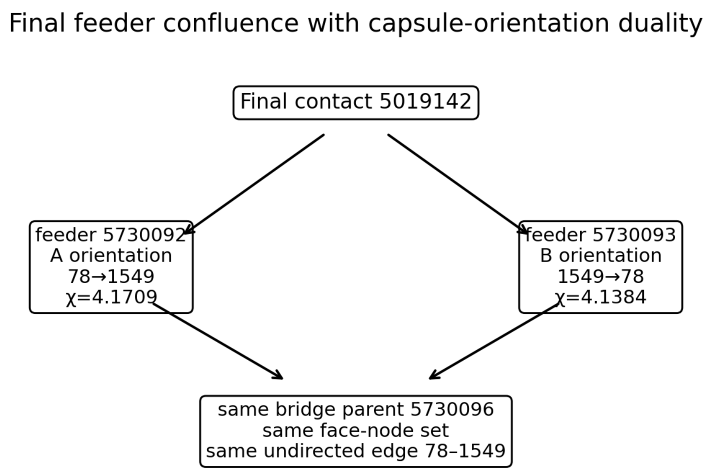

Figure 6: Final-feeder confluence. The two feeder labels create the same bridge parent and undirected edge but opposite capsule orientations.

11 Post-fracture scar taxonomy

The E30 fracture has three separable channels (Fig. 7). First, the global capacity law is the zero-anchor funnel. Second, the upstream B-side hub-knot at shell node 866 is a route-memory resonance proxy. Third, the final bottleneck scar is the 78–1549 edge family.

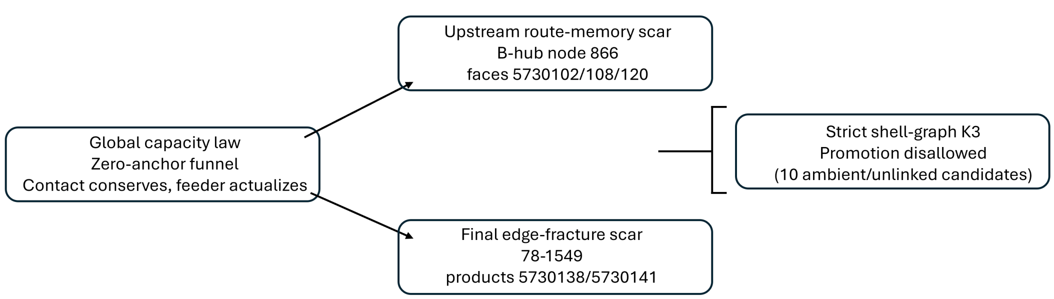

Figure 7: Three-channel scar taxonomy. The upstream B-hub at 866 and final edge-fracture scar at 78–1549 are distinct channels; strict shell-graph K3 promotion remains disallowed.

11.1 Upstream B-hub route-memory scar

The tracked B-side carrier-face hub-knot consists of faces

$$5730102, \quad 5730108, \quad 5730120. \tag{26}$$

Each is an active $C = (0, 1, 2)$ carrier. Their shell edges are

$$866\text{–}786811, \quad 866\text{–}1142509, \quad 866\text{–}1479203, \tag{27}$$

which form a carrier-face line-graph hub-knot at shared shell node 866. K11C3 maps the three target faces back to origin bridge parents 5730018, 5730030, and 5730054, at route steps 2, 4, and 8, with origin edges 173–866 and 91–866. This is an upstream route-memory scar, not final bottleneck debris.

The persistence of node 866 matters because it is an event-local correlation that survives fracture and bounded relaxation. A continuum description can certainly encode correlations, but the CD mechanism supplies a concrete graph locus at which the route memory is stored: repeated bridge edges increment a shared shell hub, and later debris inherits that hub-node label.

11.2 Final edge-fracture scar

K11C4 localizes the final bottleneck scar to the 78–1549 edge family. The final edge-family bridge parents are 5730090 and 5730096. After fracture, two active products inherit the final edge nodes:

$$5730138 \text{ on node } 78, \qquad 5730141 \text{ on node } 1549. \tag{28}$$

The product 5730138 is a pre-final edge-fracture scar from parent 5730090, while 5730141 is the final closure fracture scar from parent 5730096. These products are active carrier scars, not strict baryon detections.

11.3 Relaxation/cooling lower bound

K11C5 lets the exact E30 post-fracture state evolve for 5,000 undriven uniform relaxation steps. The B-hub seed faces remain active carrier capsules, preserve the same line-graph proxy at shared node 866, do not become a strict shell-graph K3, and produce zero strict cooling hits. Figure 8 summarizes this bounded lifetime assay.

The safe language is therefore: the 866 B-hub is a metastable upstream carrier-face resonance proxy with a 5,000-step immediate-relaxation lower bound. It is not a proved eternal bound state.

12 Strict K3/baryon guardrail

The live post-fracture shell graph contains global strict shell-graph K3 candidates, but K11C1 finds that all ten are ambient or unlinked: zero collision-born lineage passes, zero exact-frontier locality passes, and zero B-hub locality passes. K11C2 and K11C3 likewise find no strict shell-graph overlap for the tracked B-hub target. Consequently, this manuscript does not claim strict shell-graph baryon detection. The terms used here are intentionally weaker: carrier-face line-graph hub-knot proxy, upstream route-memory resonance proxy, and final edge-fracture scar.

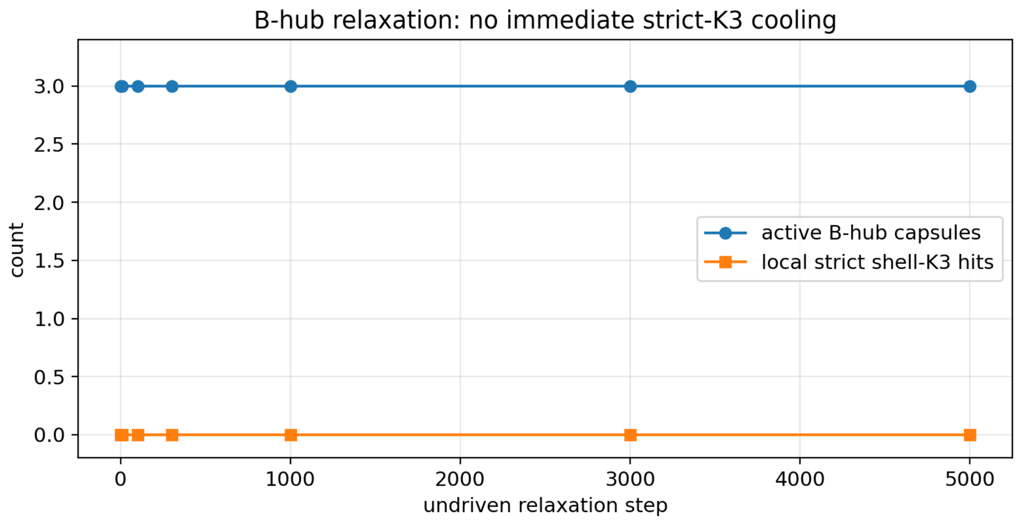

Figure 8: B-hub relaxation assay. Across 5,000 undriven steps, the 866 line-graph resonance proxy persists and no local strict shell-graph K3 cooling hit appears.

13 Finite-count cosmological baseline and falsifier

The reduced carrier vacuum is not a continuum mode sea. As a finite-count closure hypothesis, use the graph-count anchor $\log_{10} N_{\text{today}} = 122$ and the de Sitter area relation

$$N_{\text{today}} \sim \frac{R_\Lambda^2}{\ell_P^2}, \qquad R_\Lambda^2 = \frac{3}{\Lambda}. \tag{29}$$

This gives

$$\Lambda_0 = \frac{3}{10^{122}\ell_P^2} = 1.1484 \times 10^{-52}\,\mathrm{m}^{-2}. \tag{30}$$

Using $H_0 = 67.4\,\mathrm{km\,s^{-1}\,Mpc^{-1}}$ and $\Omega_\Lambda = 0.685$ as a flat-ΛCDM comparison anchor gives $\Lambda_{\Lambda\mathrm{CDM}} \simeq 1.0909 \times 10^{-52}\,\mathrm{m}^{-2}$, so the raw finite-count estimate is high by

$$\frac{\Lambda_0}{\Lambda_{\Lambda\mathrm{CDM}}} = 1.052718776. \tag{31}$$

Since $\Lambda \propto N^{-1}$, this is the required effective area multiplier,

$$F_{\text{req}} = 1.052718776. \tag{32}$$

The closure uses two multiplicative factors. We state their status explicitly because this is the most exposed numerical claim in the manuscript. The open-to-mature registry factor

$$F_{\text{reg}} = \frac{124}{120} = 1.033333333 \tag{33}$$

was locked in the open-registry cosmology branch before this carrier-density calculation was applied. The carrier-sea factor

$$F_C = 1 + \rho_C = 1.01909246 \tag{34}$$

was measured from the reduced-sector foam run before being multiplied against the residual. Their product is

$$F_{\mathrm{reg}}F_C = 1.053062209, \tag{35}$$

which differs from F_{req} by about 3.26×10^{-4} in fractional Λ residual after correction. Figure 9 shows the correction ledger.

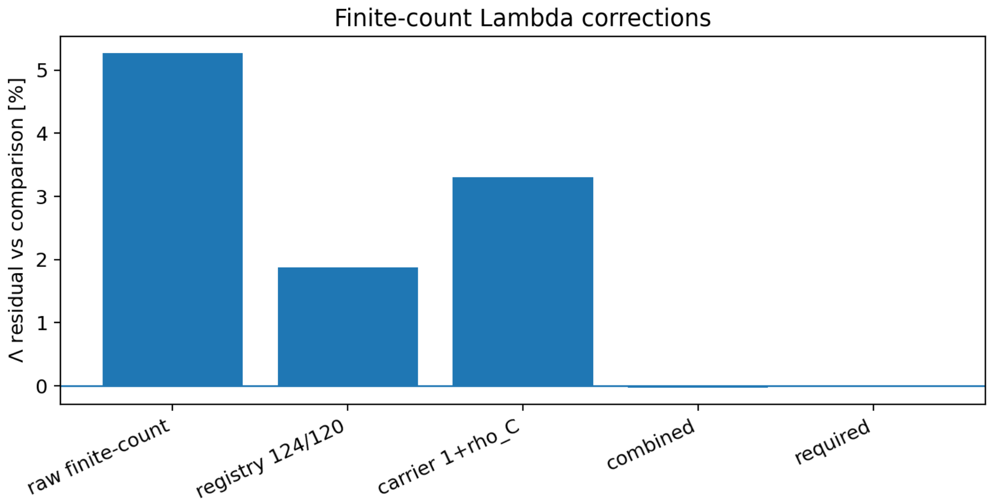

Figure 9: Candidate finite-geometry corrections to the raw finite-count Λ baseline. The combined registry and carrier factor nearly closes the comparison residual. This figure should be read as a locked-input closure test, not as a free two-parameter fit.

This is falsifiable. If longer reduced-sector runs at 10^7 or 10^8 rounds move the stable carrier density away from $\rho_C \simeq 0.019$, or if the hub variable $f_{\mathrm{hub}} = 1 - 1/d_{\mathrm{max}}$ stops approaching the closure surface, the near-closure in Fig. 9 should be rejected. The artifact bundle should eventually be replaced by a stable public archive/DOI; until then, the manuscript treats these as reproducible internal ledgers rather than referee-grade external data deposition.

14 Scope, Methodological Boundaries, and Falsifiability

To ensure the Distinction Combinatorial framework is evaluated precisely on its mechanical claims, we explicitly define the boundaries and falsification criteria of the present study.

14.1 Framework vs. Continuum QFT

This manuscript proposes a graph-mechanical architecture for how a finite discrete vacuum routes, retains memory, and fractures. It does not claim to derive a Standard Model particle from first principles, fit a collider distribution, or compute a detector-level cross-section. The collider context is utilized strictly as a macroscopic proxy comparison to demonstrate that the discrete CD natively produces the structural asymmetries characteristic of high-energy scattering.

14.2 The Strict K_3 Guardrail and Resonance Proxies

While the live post-fracture shell graph contains global strict shell-graph K_3 candidates, all ten candidates identified in this study are ambient or unlinked, possessing zero collision-born lineage.

Consequently, this manuscript does not claim a strict shell-graph baryon detection. The E_{30} collision scars—specifically the upstream B-side 866 hub—are classified as highly excited carrier-face resonance proxies. The $5,000$-step bounded relaxation assay confirms these proxies are metastable, establishing that the local vacuum must cool further before proto-baryonic fragments can collapse into strict shell-graph ground states.

14.3 Channel Specificity

The E_{30} soft-wall transition is reported as a channel-specific result, derived from the successful primary $11 + 4$ channel. Alternate dynamic decompositions tested in this study failed to reach the strict $15C_{\mathrm{AB}}$ bridge peak due to unavailable current zero-anchor replacements. Therefore, we do not claim decomposition-invariant behavior at the E_{30} threshold; rather, we demonstrate that navigating vacuum congestion at this energy scale requires highly specific topological routing.

14.4 Cosmological Falsifiability

The cosmological baseline calculation is a locked-input closure derivation. It relies strictly on the open-to-mature registry factor and the microscopic carrier density ($\rho_C \simeq 0.019092$) measured natively within the reduced-sector foam run. This derivation is explicitly falsifiable: if future reduced-sector runs at 10^7 or 10^8 rounds demonstrate that the stable carrier density drifts away from $\rho_C \simeq 0.019$, or if the shell-hub condensation proxy fails to approach the closure surface, the near-closure of the Λ residual presented in this manuscript must be rejected.

15 Discussion

The main result is a graph-theoretic lifecycle of a discrete high-energy fracture. The finite carrier sea supplies the vacuum medium. The zero-anchor capacity funnel supplies the interaction-space boundary condition. The upstream 866 hub scar records route memory. The final 78–1549 edge scar records the localized failure coordinate where depleted capacity actualizes. This makes the E30 near-wall channel more than a phenomenological pattern: it is a two-stage graph-capacity mechanism.

A useful comparison is a hypothetical distributed-fracture model. In such a model, one would expect bridge capacity to fail over many edge families, contact ranks to vary as the route explores alternatives, and zero-anchor depletion to be nonlinear or stochastic. The E30 primary channel shows the opposite signature: every selected contact is rank zero, the pool drains linearly, no product edge is removed during bridge formation, and the final failure localizes to a single edge family. This does not prove that all high-energy CD collisions behave this way, but it gives a clear observable signature for future impact-parameter tests.

The route-memory scar at 866 is also nontrivial. It separates memory from immediate fracture: node 866 is inherited from earlier route steps $2, 4, 8$, while the final bottleneck is 78–1549. The $5,000$-step relaxation assay further shows that the 866 resonance proxy does not immediately cool into a strict shell-graph K_3 or disappear. Thus, route history can remain localized in the carrier shell even after the final edge fracture has occurred.

The final-feeder confluence is the most physics-flavored internal result. The two final feeder choices produce the same bridge parent and undirected edge but opposite capsule orientation and different χ_{km} values. This suggests a concrete next test for a CD analogue of helicity: branch the post-peak state by final feeder orientation and ask whether later interactions are orientation-selective.

16 Conclusion: The Unified Signature of a Discrete Graph Universe

Standard continuum approximations are currently reaching their structural limits across multiple observational regimes, struggling to accurately model non-perturbative hadronization at the TeV scale [1, 5, 6] and consistently map high-precision cosmological expansion [7, 11]. The Distinction Combinatorial (DC) framework addresses these fundamental limits by modeling physical reality not as a continuous geometric background, but as a discrete relational graph emerging from a primordial logical substrate [12, 13].

At the microscopic scale, we propose that the vacuum operates as a hard-core sea of self-reproducing carrier capsules rather than a continuous mode field. High-energy scattering does not represent a stochastic failure of a continuum, but the deterministic execution of relational graph actualizations within a depleted, finite zero-anchor capacity funnel. The resulting topological artifacts—specifically the upstream 866 hub route-memory proxy and the final 78-1549 edge fracture—suggest that the interaction space of the universe is fundamentally discrete and mechanically constrained.

The code repository for reproducibility is located here: `https://github.com/jrmerwin/finite_carrier_foam.git`

References

[1] CMS Collaboration. Search for high mass dijet resonances with a new background prediction method in proton-proton collisions at $\sqrt{s} = 13\,\mathrm{TeV}$. 2019.

[2] CMS Collaboration. Search for new physics in dijet angular distributions using proton-proton collisions at $\sqrt{s} = 13\,\mathrm{TeV}$ and constraints on dark matter and other models. *European Physical Journal C*, 78:789, 2018. doi: 10.1140/epjc/s10052-018-6242-x.

[3] CMS Collaboration. Measurement of dijet angular distributions and search for beyond the standard model physics in proton-proton collisions at $\sqrt{s} = 13\,\mathrm{TeV}$. 2026.

[4] Richard P. Feynman and Albert R. Hibbs. *Quantum Mechanics and Path Integrals*. McGraw-Hill, 1965.

[5] Michael E. Peskin and Daniel V. Schroeder. *An Introduction to Quantum Field Theory*. Westview Press, 1995.

[6] Steven Weinberg. *The Quantum Theory of Fields, Volume 1: Foundations*. Cambridge University Press, 1995.

[7] Planck Collaboration, N. Aghanim, et al. Planck 2018 results. vi. cosmological parameters. *Astronomy & Astrophysics*, 641:A6, 2020. doi: 10.1051/0004-6361/201833910.

[8] M. Abdul Karim et al. DESI DR2 Results II: Measurements of Baryon Acoustic Oscillations and Cosmological Constraints. 2025. DESI Collaboration.

[9] D. Scolnic et al. The pantheon+ analysis: The full data set and light-curve release. *Astrophysical Journal*, 938:113, 2022. doi: 10.3847/1538-4357/ac8b7a.

[10] D. Brout et al. The pantheon+ analysis: Cosmological constraints. *Astrophysical Journal*, 938:110, 2022. doi: 10.3847/1538-4357/ac8e04.

[11] A. G. Riess et al. A comprehensive measurement of the local value of the hubble constant with $1\,\mathrm{km\,s^{-1}\,Mpc^{-1}}$ uncertainty from the hubble space telescope and the sh0es team. *Astrophysical Journal Letters*, 934:L7, 2022.

[12] Jason Merwin. Mature 137-registry carriers and particle-like excitations in an open-token distinction engine. *viXra*, 2604.0103, 2026.

[13] Jason Merwin. Geometric origin of fundamental constants: Thirty derivations from discrete relational structure and the substrate-interface duality. *viXra*, 2605.0023, 2026.